Materials Science and Engineering B 304 (2024) 117376

Contents lists available at ScienceDirect

Materials Science & Engineering B

journal homepage: www.elsevier.com/locate/mseb

Characterization of quasiparticle relaxation times in microstrips of NbReN for perspective applications for superconducting single-photon detectors

Z. Makhdoumi Kakhaki [a], A. Leo [b], A. Spuri [c], M. Ejrnaes [d], L. Parlato [e], G.P. Pepe [e], F. Avitabile [b], A. Di Bernardo [a,c], A. Nigro [a], C. Attanasio [a,*], C. Cirillo [b]

[a] Dipartimento di Fisica "E. R. Caianiello", Università degli Studi di Salerno, 84084 Fisciano (Sa), Italy
[b] CNR-SPIN, c/o Università di Salerno, Via Giovanni Paolo II, 132, 84084 Fisciano (Sa), Italy
[c] Universität Konstanz, Fachbereich Physik, Universitätsstraße 10, 78457 Konstanz, Germany
[d] CNR-SPIN, Via Campi Flegrei, 34, 80078 Pozzuoli (Na), Italy
[e] Dipartimento di Fisica "E. Pancini", Università degli Studi di Napoli Federico II, 80125 Napoli, Italy

ARTICLE INFO

Keywords:
NbReN microstrips
Flux-flow instability
Quasiparticle relaxation time
Superconducting single-photon detectors

ABSTRACT

The study of the flux-flow instability in superconducting materials has recently gained renewed attention due to its potential implications for the use of the analyzed materials as micrometer-sized superconducting detectors for single photons. The values of the quasiparticle relaxation time (τ_E) measured for these detectors are affected by pinning properties. Here, we report electric transport properties of NbReN microstrips of different quality. For the strip characterized by high resistivity, and large critical currents and pinning, we estimate a value of τ_E that is almost two orders of magnitude larger compared to that of another strip with a smaller value for the critical current, for which we measure $\tau_E \sim 12$ ps. This low value is comparable to those reported in the literature for microstrips made of other highly-disordered superconductors. Our results suggest that NbReN microstrips have great potential for the realization of superconducting single-photon detectors, depending on further optimization of their fabrication process and the superconducting properties affected by it.

1. Introduction

Superconducting nanostrip single-photon detectors (SNSPDs) are advanced detectors of single photons operating mainly in the near-infrared region with high efficiency and low noise [1–5]. They have found applications in various fields of quantum technologies, including quantum optics, communication, and computation [6]. SNSPDs consist of superconducting wires (or strips) with widths of the order of tenths of nanometers, biased close to their critical current (I_c). When a photon is absorbed, the value of I_c decreases, causing the strip to switch to the normal state. As described by the "hot-spot" model, the energy released by the photon breaks the Cooper pairs creating quasiparticles that locally suppress superconductivity giving rise to a measurable voltage [7]. SNSPDs offer several advantages such as high count rates, low dark count rates (DCR), and low timing jitter [3,5,6]. Recent advancements have extended their detection capabilities to longer wavelengths, including the mid-infrared range. This has opened up new possibilities for their application also in fields like molecular spectroscopy, [8] light detection and ranging (LIDAR), [9,10] and dark matter detection [11]. Typically, SNSPDs are made from materials like NbN [12] and NbTiN [13] but amorphous (WSi, MoSi, and MoGe) [14–16] and disordered (NbRe) [17] superconductors have also been used.

Recently, the "hot-spot" model has been reformulated, suggesting that when a photon is absorbed in a type–II superconducting film, it generates vortex-antivortex pairs [18,19]. The significant implication of this reformulation is that photon detection is vortex-assisted at the initial stage of dissipation, and it is not limited to nanometer-wide strips but extends to micrometer-wide type–II superconducting strips, which are the superconducting materials from which SNSPDs are made. This extension is possible when I_c is close to I_{dep}, where I_{dep} represents the depairing current. The ratio I_c/I_{dep} depends on the properties of the superconducting material, particularly on the values of the electronic and phononic specific heats [19,20]. Additionally, the width of the strip (w) must be smaller than the Pearl length $\Lambda = 2\lambda^2/d$. Here λ is the magnetic field penetration depth and d is the thickness of the strip. This prediction was largely confirmed by experiments since the photon detection was successful also in superconducting microstrip single-photon detectors (SMSPDs) made from different materials [20–28].

One successful method used to determine whether a superconducting material is suitable for SMSPDs is the study of the flux-flow

* Corresponding author.
E-mail address: cattanasio@unisa.it (C. Attanasio).

https://doi.org/10.1016/j.mseb.2024.117376
Received 18 March 2024; Received in revised form 10 April 2024; Accepted 15 April 2024
Available online 19 April 2024

Table 1
Values of some characteristic parameters of the NbReN microstrips. L is the distance between the voltage contacts, w is the width of the microstrip, and d its thickness. ρ is resistivity in the normal state at the temperature just above the superconducting transition, while T_c is the critical temperature. $\Lambda(0)$ is the Pearl length at zero temperature, and $\lambda(0)$ represents the magnetic field penetration depth at zero temperature.

Sample	L (μm)	w (μm)	d (nm)	ρ (μΩ cm)	T_c (K)	$\Lambda(0)$ (μm)	$\lambda(0)$ (μm)
D2	90	2	20	511	4.2	134	1.16
D10	90	10	7.5	300	4.4	200	0.87

instability (FFI) by transport measurements, [29–35] since to have a fast photoresponse in SMSPDs it is crucial that the superconductor can sustain a high velocity of the vortices [36]. In this context, the quasiparticle relaxation time (τ_E) is a key parameter. τ_E is obtained by analyzing the current (I) – voltage (V) characteristics in the presence of a perpendicular magnetic field ($B = \mu_0 H$) within the framework of the Larkin–Ovchinnikov (LO) theory, [37] and it provides valuable insights into the suitability of the superconducting material for SMSPDs [32–34, 38–40].

Due to the good performances of NbRe-based SNSPDs especially in terms of time resolution, [17] thin films of NbRe nitride (NbReN) have been recently synthesized with the aim of improving some of the main figures of merit of the devices [33]. In particular, its reduced gap and enhanced resistivity suggest testing NbReN as an alternative material to amorphous superconductors for the realization of SMSPDs. We anticipate that NbReN-based devices should exhibit a faster response compared to those based on amorphous superconductors. Reduced values of τ_E, comparable to those extracted for NbRe, were indeed obtained from a preliminary characterization. However, the effect of disorder and pinning on the transport properties of the material deserves deeper investigation [33].

In this work, we analyze the vortex lattice instability in microstrips of NbReN to better explore the material's tunability for future applications. We measured transport properties in the presence of a magnetic field down to a temperature of 2 K and found that the value of τ_E strongly depends on the quality of the strips in terms of pinning and conductivity. Additionally, the geometrical characteristics and thickness of the strips also affect the quasiparticle relaxation time. Larger values for τ_E are obtained for the thick and narrow strip, characterized by a larger critical current density.

2. Experimental and samples characterization

Two NbReN thin films were deposited on SiO_2 substrates by dc reactive sputtering in a ultra-high vacuum (UHV) system, starting from a stoichiometric 2-inch-diameter $Nb_{0.18}Re_{0.82}$ target. The base pressure in the chamber was 2×10^{-8} mbar, and the deposition was performed in a mixture of Ar and N_2 gases. The total pressure was $P_{tot} = 3.5 \times 10^{-3}$ mbar, with a N_2 percentage of 15% of P_{tot}, and a power of 350 W. This resulted in a deposition rate of 0.37 nm/s. The resulting films had thicknesses (d) of 7.5 nm (sample D10) and 20 nm (sample D2). Subsequently, they were patterned by optical lithography into a four-probe geometry with a distance of $L = 90$ μm between the two voltage contacts and a width of $w = 10$ μm for sample D10 and 2 μm for sample D2. Sample D10 was obtained by additive patterning, involving the design of the device geometry using a polymeric positive resist spin-coated onto the substrate. The NbReN film was then deposited, and the polymer was removed by lift-off, which may produce an undercut profile. In contrast, sample D2 was patterned by using direct writing via a microprinter. Subsequently, the pattern was transferred to the superconducting layer using argon ion etching, with a dig rate of 1 nm/min. The argon pressure and beam power were maintained at 2.8 mTorr and 5 W, respectively. This technique results in microstrips with straight edges, ensuring the uniform width of the device. For sample D2, the microstructuring procedure was conducted a few weeks after

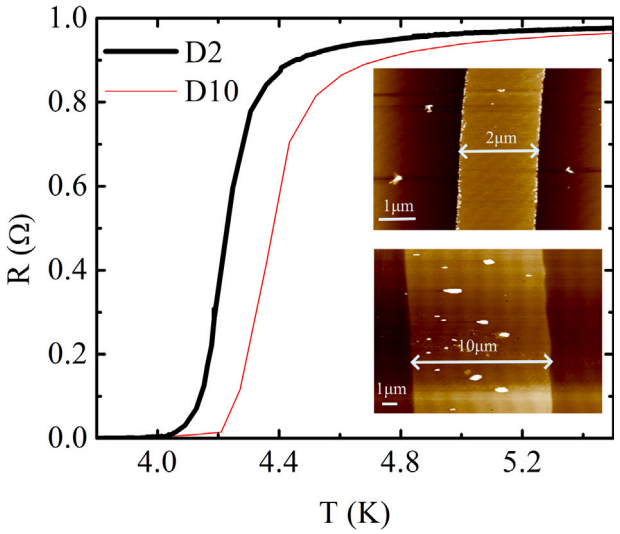

Fig. 1. Zero-field resistive transitions of the two microstrips. The insets show the AFM image of the microstrip D2 (upper panel) and D10 (lower panel).

the sputtering deposition. The insets of Fig. 1 display the Atomic Force Microscope (AFM) image of both microstrips. Transport measurements were carried out in a Cryogenic Ltd. CFM9T cryogen-free system. Resistive transitions were conducted in current-biased mode with bias current $I_b = 10$ μA. I–V curves were measured by applying rectangular current pulses to the samples for 2.5 ms with a current-off period of 2 s. Voltage measurements were acquired at the maximum current value, and this process was repeated by sweeping the current both upward and downward. The absence of hysteresis in the curves indicates that thermal heating did not affect the measurements. Fig. 1 presents the resistive curve for both microstrips D2 and D10 in the absence of a magnetic field. The critical superconducting temperature, measured at the midpoint of the transition, is $T_c = 4.2$ K for D2 and 4.4 K for D10. These values are substantially consistent with the T_c of a patterned film of the same thickness, [33] indicating that the lithographic process did not adversely affect the bridge properties. The low-temperature resistivity (ρ) was 511 μΩ cm for sample D2 and 300 μΩ cm for sample D10. Both values are higher than those previously reported for unpatterned films, which were also grown under different conditions [33]. The particularly large value of ρ in microstrip D2, along with the slightly depressed value of T_c, may be partially attributed to the aging process that the device has been exposed to. Using for the magnetic field penetration depth at zero temperature the relation $\lambda(0) = 1.05 \times 10^{-3} \sqrt{\rho / T_c}$, [41] we find that for sample D2, $\lambda(0) = 1.16$ μm and $\Lambda(0) = 134$ μm, (the Pearl length at zero temperature). For microstrip D10, we have $\lambda(0) = 0.87$ μm and $\Lambda(0) = 200$ μm. The zero-temperature in-plane coherence length $\xi(0)$ has been taken equal to 7.2 nm for both samples [42]. This value is obtained from the measured perpendicular upper critical magnetic field of a 10-nm NbReN strip specifically prepared for this kind of investigation. $\mu_0 H_{c2}(0)$ is estimated using the Werthamer, Helfand, and Hohenberg (WHH) theory for the temperature dependence of the critical field, [43] followed by the simple relation $\mu_0 H_{c2}(0) = \phi_0 / [2\pi\xi(0)^2]$, with $\phi_0 = 2.07 \times 10^{-15}$ Wb being the flux quantum. For both bridges, it holds that $\xi(0) \ll w \ll \Lambda(0)$. A summary of the sample properties is presented in Table 1.

3. Current–voltage characteristics and critical currents

The I–V characteristics have been measured at different temperatures and fields for both microstrips. The external field H has always been applied perpendicularly to the plane of the substrate. I–V curves for the both microstrips measured at $T = 2$ K for different fields

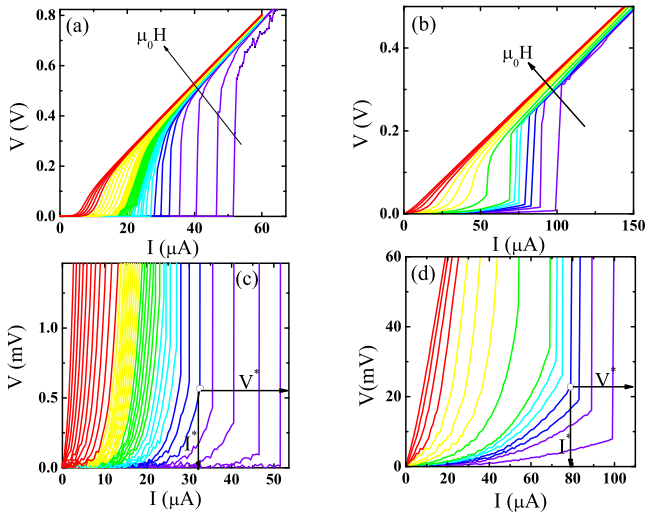

Fig. 2. (a) Representative of I–V curves of the microstrip D2 at $T = 2$ K in different magnetic fields from 10 mT to 4 T. (b) The same as panel (a) for the microstrip D10 in different magnetic fields from 10 mT to 5 T. (c) Enlarged plot in the low-voltage regime of panel (a) to show the nonlinear conductivity regime and the instability jumps. The point marked on these plots is denoted by coordinates I^* and V^*, representing the instability current and voltage, respectively. (d) Enlarged plot in the low-voltage regime of panel (b).

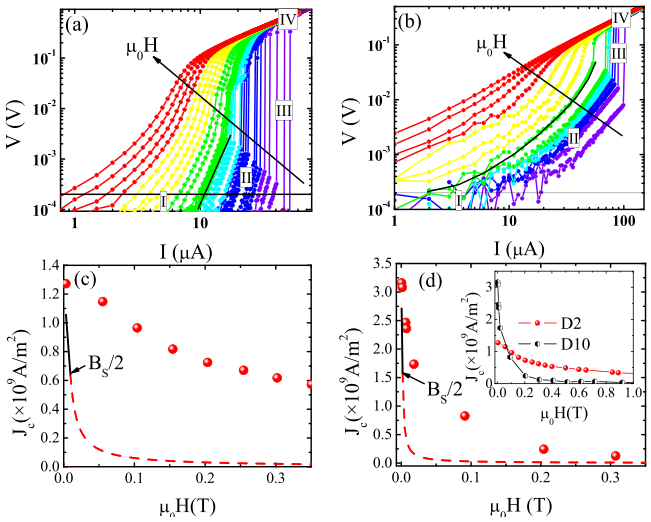

Fig. 3. (a) Log–log plot of the same data shown in Fig. 2(a). The three different regimes in the superconducting state are indicated: pinned vortices (I), nonlinear motion of the vortices (II), instability of the vortex velocity (III). IV indicates the normal state region. The solid line shows the nonlinear regime of conductivity before the jump to the normal-state. (b) Log–log scale plot of the same data shown in Fig. 2(b). (c) Magnetic field dependence of the critical current density at $T = 2$ K of the sample D2. The black solid line shows the linear behavior for the critical current density, as obtained according to Eq. (1) for $B \leq B_s/2$. For $B > B_s/2$, the red dashed line represents the curve $J_c(B) \propto B^{-0.5}$. (d) The same as panel (c) for the sample D10. The inset shows the values of J_c for both the microstrips up to 1 T.

are presented in Fig. 2(a) and Fig. 2(b). For clarity, only the upward sweep is shown. All the curves show a regime of zero voltage at small bias currents where vortices are pinned. As the current is further increased, a nonlinear conductivity regime is present until a certain current I^* where the instability jump to the normal state takes place. The corresponding voltage is denoted as V^*. As the magnetic field is increased, the discontinuity in the transition disappears, and the return to the normal state occurs continuously, as better shown in Fig. 2(c) and Fig. 2(d). Recent observations have indicated that, although the study of the instability provides a good indication of the superconducting material's potential effectiveness as a single-photon detector, a more precise evaluation of τ_E from the I–V curves necessitates a careful examination of the microstrip edges' quality [36]. Specifically, a more rigorous determination of quasiparticle relaxation times can only be achieved if vortices are predominantly pinned at the edge of the strip. AFM images of samples D2 and D10 (insets of Fig. 1) show that the edge quality of the two samples is similar, although the edges of sample D2 appear sharper.

Since the magnetic field dependence of the critical current density ($J_c = I_c/wd$) offers insights into the mechanisms at play in different regimes, [24,34,36,44–46] the $J_c(B)$ behavior has been first analyzed for the two samples. The maximum current density that a superconductor can sustain at zero magnetic fields is the depairing current density, J_{dep}. When the field is increased and vortices start to enter the sample, the critical current density is determined by the penetration and movement of magnetic vortices. At low magnetic fields, in the Meissner state, the critical current density is dominated by the vortex penetration at the edges of the strip and $J_c \propto J_{edge} \propto (1 - B/B_s)$, where the field B_s depends on the material and the geometry of the strip through the relation $B_s(T) = \phi_0/(\sqrt{3}\pi\xi(T)w)$, valid for $\xi(T) \ll w \ll \Lambda(T)$ [36,47]. When the field is further increased over $B_s/2$, the volume pinning is the main factor that determines the critical current density and $J_c \propto J_{pin} \propto B^{-0.5}$ [47]. The actual value of J_c corresponds to the larger value between J_{edge} and J_{pin}. In the panel (a) [(b)] of Fig. 3 the I–V characteristics of the panel (a) [(b)] of Fig. 2 are shown in a log–log plot. The horizontal line in the plots marks the voltage criterion chosen to extract the value of I_c, taken at $V = 200$ μV. This value is far out from the noise region of the I-V curves and allows to determine I_c significantly. In the panel (c) [(d)] of Fig. 3 we show the magnetic field dependence of J_c at $T = 2$ K for the sample D2 (D10). In the same figures, using the characteristic values of the two samples, the quantity

$$J_c(B,T) = J_c(0)[1 - B/B_s(T)] \quad (1)$$

is plotted as a continuous black solid line for $T = 2$ K and for $B \leq B_s/2$. $B_s/2 \sim 9.5$ mT for sample D2 and ~ 2 mT for the strip D10. The red dashed line shows the dependence $J_c(B) \propto B^{-0.5}$ valid for $B > B_s/2$. In both cases, the plotted lines are notably distant from the experimental data points, although the low-field data of microstrip D10 are closer to the theoretical predictions. At small fields, J_c for sample D10 is more than a factor two larger than that for sample D2. The measured values of J_c at $B \leq B_s/2$ indicate that the edge barrier does not significantly affect vortex entry in both samples. This suggests that neither the lift-off nor Ar-etching procedures yield high-quality edges, resulting in a reduced barrier for vortices to enter the samples. It is evident that edge pinning has a negligible effect, and volume pinning primarily contributes to the value of J_c in both strips. At high fields, the $J_c(B)$ curves of the two samples intersect, as shown in the inset of Fig. 3(d). Notably, the values of J_c for sample D2 exceed those for sample D10, indicating stronger volume pinning for sample D2 at high fields. This result is confirmed by examining the behavior of the flux-pinning force density, $F_p = J_c\mu_0 H$, as a function of the magnetic field, as shown in Fig. 4(a). Both at 2 K and 3 K, D2 exhibits a significantly larger F_p compared to D10. Fig. 4(b) shows the reduced flux pinning force, $f_p = F_p/F_p^{max}$ (F_p^{max} is the maximum value of the flux-pinning force density at each temperature), as a function of the reduced magnetic field, $h = H/H^*$. Here, we define $\mu_0 H^*$ as the field at which $J_c = 1 \times 10^6$ A/m^2 at a certain temperature. In the absence of a direct measurement of $\mu_0 H_{c2}$, using a lower normalization field has proven successful in obtaining information about the behavior of the reduced pinning force in superconducting materials [48–51]. In both samples, the data exhibit a clear scaling behavior, with data points at the two temperatures falling along the same curve. This alignment indicates the presence of the same pinning mechanism in both microstrips at low temperatures. The value of the reduced field, denoted as $\tilde{h}$, where

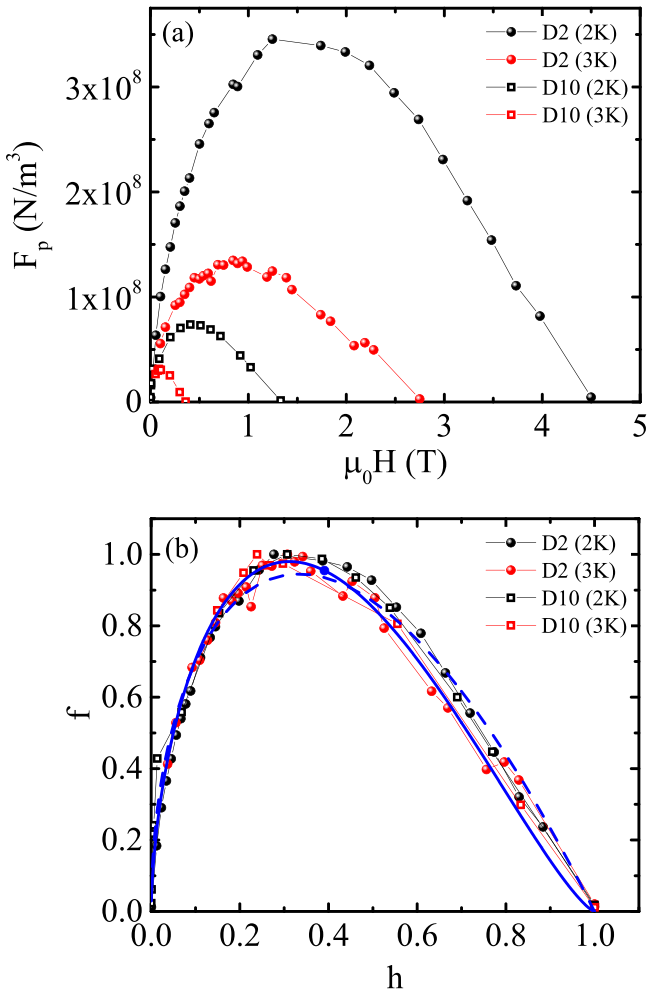

Fig. 4. (a) Pinning force density as a function of the magnetic field at $T = 2$ K and $T = 3$ K for sample D2 (open and closed circles) and D10 (open and closed squares). (b) Reduced pinning force density as a function of the reduced field at $T = 2$ K and $T = 3$ K for sample D2 (open and closed circles) and D10 (open and closed squares). The solid line is the best fit to the data of sample D2 with the formula $f \propto h^{0.6}(1-h)^{1.33}$. The dashed line is the curve $f \propto h^{0.5}(1-h)$.

f reaches its maximum, is equal to 0.31. In Fig. 4(b), the solid line represents the best fit to the data using the relation $f \propto h^p(1-h)^q$ with estimated values of $p = 0.60 \pm 0.02$ and $q = 1.33 \pm 0.03$. Notably, these values do not align with established expressions for flux-pinning in type-II superconductors [52]. However, the $f(h)$ curve obtained fixing $p = 0.5$ and $q = 1$, valid for volume pinning, [52] closely approximates to the best-fitting curve and is represented by the dashed line in Fig. 4(b). In this case, $\tilde{h} = p/(p+q)$ is 0.33. Furthermore, the data for sample D10 exhibit a different scaling law compared to a previous report, carried out on strips with the same width [33]. This deviation in behavior may be attributed to the presence of inhomogeneities, as evidenced by the extended tail in the reduced pinning force at high reduced fields [33]. However, these observed differences may not only result from variations in the quality of samples grown under different conditions but also from discrepancies in the definition of H^* in the two cases.

From the previous analysis, it results that in the samples under study, a strong pinning is present. In this case, the shape of the I–V characteristics is modified with respect to the LO expression [37] and in the high–voltage region the nonlinear curves can be better described

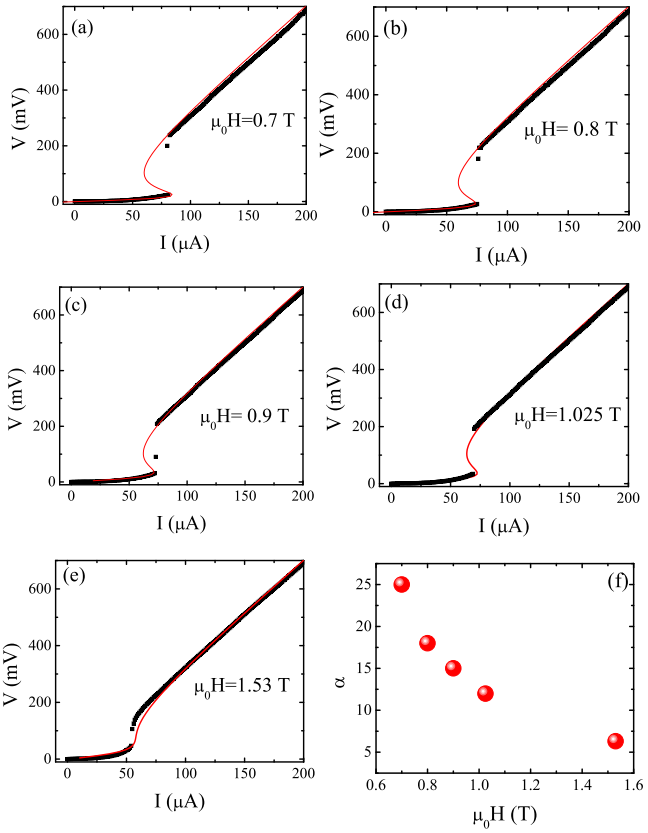

Fig. 5. (a)–(e) I–V curves for microstrip D10 for selected values of the magnetic field at $T = 2$ K. The solid lines are the fits to the experimental data by Eq. (2). (f) Magnetic field dependence of the fitting parameter α.

by [53,54]

$$I = \frac{V}{R_N}\left[\frac{\alpha(1+\beta V^{-c})}{1+(V/V^*)^2}+1\right] \tag{2}$$

where R_N is the normal state resistance. The parameter α has been introduced to correct the flux-flow resistivity in the limit of low voltage, [55] while parameters β and c describe the renormalization of the vortex viscosity in the LO theory [37] due to the strong pinning [53]. As in the LO theory, I as a function of V is N–shaped [37,53,55]. When the sample is current-biased, as in our experiment, the I and V axes should be exchanged, resulting in an S-shaped curve. Consequently, when the current reaches the value at which the slope of the I–V curve changes sign in the voltage-biased mode, instability occurs, and the system jumps to the normal state [55]. In panels (a)–(e) of Fig. 5, we present I–V curves at various fields at $T = 2$ K for sample D10. The red solid lines represent fits to the data using Eq. (2), with α, β, and c as free parameters. It is evident that Eq. (2) effectively describes the experimental data across the entire range. As shown in panel (f) of Fig. 5, α is around 25 at small fields, and, as expected, it decreases as the field increases, since the I–V curves become more smeared and the jump tends to disappear making the non-linear effects in the curves less significant. The values of β are of the order of 5×10^{-2} and c is in the range 0.7–1. These results well match with what has been previously reported in the literature on high-pinning multilayers [53]. On the contrary, data for microstrip D2 (not shown here) are not well reproduced by Eq. (2), particularly in capturing the non-linear region of the I–V characteristics before the jump, even when using very large values of the parameter α. As we will discuss further below, all these results affect the determination of the values of τ_E [36].

Finally, we compare the measured value of J_c with the expected J_{dep} for the two microstrips. At $T = 0$ and for strips that are both thin and

Table 2
Calculated values of J_{dep} at both zero temperature and 2 K, as well as J_c measured at $T = 2$ K and $\mu_0 H = 10$ mT. The ratios J_c/J_{dep} and J^*/J_c are also reported.

Sample	$J_{dep}(0)$ (A/m^2)	$J_{dep}(2\,K)$ (A/m^2)	$J_c(2\,K)$ (A/m^2)	$J_c(2\,K)/J_{dep}(2\,K)$	$J^*(2\,K, 0.5\,T)/J_c(2\,K, 0.5\,T)$
D2	2.85×10^{10}	1.41×10^{10}	1.27×10^{9}	0.07	1.25
D10	5.21×10^{10}	1.47×10^{10}	3.16×10^{9}	0.21	15

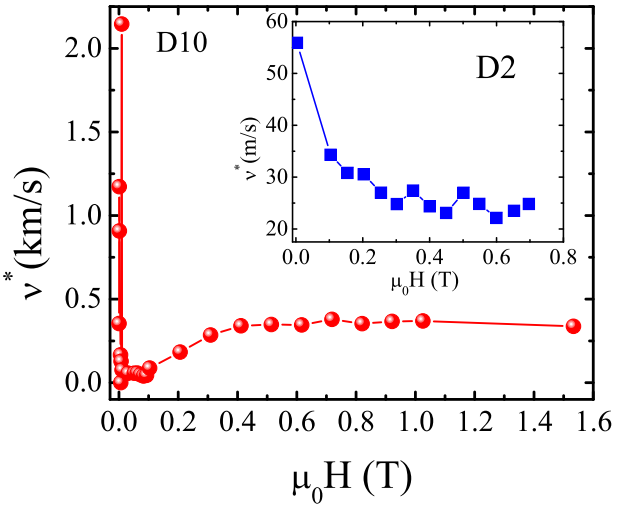

Fig. 6. Critical velocity of the microstrip D10 as a function of the external magnetic field at $T = 2$ K. Inset: The same as in the main panel for the microstrip D2.

wide it is [56]

$$J_{dep}(0) = \frac{8\pi^2\sqrt{2}\pi}{21\zeta(3)e}\sqrt{\frac{(k_B T_c)^3}{\hbar v_F \rho(\rho\ell)}} \tag{3}$$

where v_F is the Fermi velocity, ℓ electronic mean free path and $\zeta(x)$ is the Riemann zeta function. The comparison with the measured critical current density at a certain temperature can be done rescaling the zero-temperature value to the desired value of T using the universal form of $[J_{dep}(t)/J_{dep}(0)]^{2/3}$ ($t = T/T_c$ is the reduced temperature) described by the Kupriyanov-Lukichev theory, [57] and performing the numerical calculations.

To estimate $J_{dep}(0)$ from Eq. (3) we use the measured values of ρ and T_c for the two samples. Regarding the microscopic parameters of the two microstrips, we consider [33] $\ell = 0.5$ nm and $\tau = 1.2 \times 10^{-15}$ s from which we obtain $v_F \sim \ell/\tau = 4.2 \times 10^5$ cm/s. In Table 2 we report the measured J_c at $T = 2$ K for the two microstrips together with the calculated values of J_{dep} at zero temperature and 2 K. For sample D10 at $T = 2$ K ($t \approx 0.5$) it is $J_c/J_{dep} = 0.27$, which is in agreement with previous results [33]. At the same temperature, we have a much smaller value $J_c/J_{dep} = 0.07$ for sample D2, indicating again that the poor quality of the strip can yield misleading information about the properties of the material.

4. Vortex critical velocity

The sudden jump of the voltage at the end of the linear flux-flow regime has been studied following the LO theory [37]. From the value of V^*, the maximum vortex velocity v^* is obtained using the relation $v^* = V^*/(\mu_0 H L)$. The theoretical LO expression for the critical velocity gives a magnetic field independent expression which is however valid only when the quasiparticle nonequilibrium distribution is spatially homogeneous [58,59]. This condition is satisfied at high fields when the quasiparticle diffusion length $\sqrt{D\tau_E}$ is larger than the intervortex distance $a_0 = \sqrt{2\phi_0/\sqrt{3}\mu_0 H}$ [58,59]. In this case, v^* only depends on the temperature through the expression [37]

$$v^* = \frac{D^{1/2}[14\zeta(3)(1 - T/T_c)]^{1/4}}{(\pi\tau_E)^{1/2}} \tag{4}$$

where $\zeta(x)$ is the Riemann zeta function and D is the quasiparticle diffusion coefficient. In Fig. 6 the critical velocity is plotted as a function of the magnetic field at $T = 2$ K for samples D10 (main panel) and D2 (inset of the figure). Microstrip D10 shows an anomalous behavior of the critical velocity at very low fields which however has been already observed in Nb strips of similar width and was attributed to nonuniform magnetic-flux penetration [60]. Using $D = 0.48 \times 10^{-4}$ m^2/s for NbReN, [33] we can estimate from Eq. (4) the values of the quasiparticle relaxation time. At $T = 2$ K and $\mu_0 H = 0.6$ T we achieve $v^* \sim 400$ m/s for sample D10 while for the narrower strip D2 a significantly lower value of $v^* \sim 15$ m/s is observed. This difference is likely related to the fact that for strip D2 the impact of the edge barrier is negligible, as demonstrated by the data reported in Fig. 3(c). Moreover, at high fields, the value of J_c is larger for sample D2 than for sample D10 [see inset of Fig. 3(d)], resulting in lower values for the critical velocity. As recently observed, an increase in the flux-flow instability velocity is caused by the degradation of NbRe films due to surface oxidation [61]. This may be the case in sample D2, where, as reported above, an aging process results in higher normal state resistivity and lower T_c. Consequently, the intrinsic relaxation time of the material is overestimated [36]. For strip D2, the resulting value of the quasiparticle relaxation time is $\tau_E \sim 20$ ns, while for sample D10 we have $\tau_E \sim 340$ ps, which is consistent with a previously reported investigation [33]. However, it is important to note that these values are influenced by the fact that the pinning due to the edge barrier is not the main mechanism of the flux-flow instabilities, even in microstrip D10. Therefore, in both samples, the obtained values of v^* significantly deviate from those measured in superconducting samples where explicit efforts were made to optimize conditions for fabricating strips with sharp edges and low roughness to increase edge pinning. These optimized conditions were aimed at achieving larger values of the critical velocity [34,36]. Moreover, the values of $v^* \sim 20$ km/s mentioned in those papers [34,36] were obtained at fields of the order of tenths of mT. In the case of sample D10, at low fields and $T = 2$ K, we measured v^* as high as 2 km/s. Given the small diffusivity of NbReN, this measurement implies $\tau_E \sim 12$ ps (see Eq. (4)).

The analysis of $J^* = I^*/wd$ also deserves some attention. In Fig. 7 the J–V curves for microstrips D2 and D10 at $T = 2$ K and $\mu_0 H = 0.5$ T are plotted in a semi-log representation. While at this field and temperature J_c is larger for sample D2 [see also inset of Fig. 3(d)], the value of J^* is larger for microstrip D10. Specifically, the ratio J^*/J_c is equal to 1.25 for sample D2 and 15 for sample D10. In general, at high fields, J^*/J_c is always smaller for sample D2. In microstrip D2, where stronger bulk pinning is at play, the instability point appears within a highly-nonlinear plastic flow regime and it is reached at a lower voltage. As predicted, lower critical velocities are measured in the presence of stronger pinning [62].

Finally, we examine the behavior of $\tau_E(T)$ as it can offer valuable insights into the relevant relaxation mechanism in play within the samples. If the dominant contribution comes from electron–electron (ee) recombination, then it is $\tau_E(T) \propto \exp[2\Delta(T)/k_B T]$, where Δ is the superconducting gap. In this case, $\tau_E(T)$ reflects the temperature dependence of the number of quasiparticles [63]. When the electron–phonon (ep) mechanism plays the main role in the recombination process, since the number of phonons decreases with temperature, we

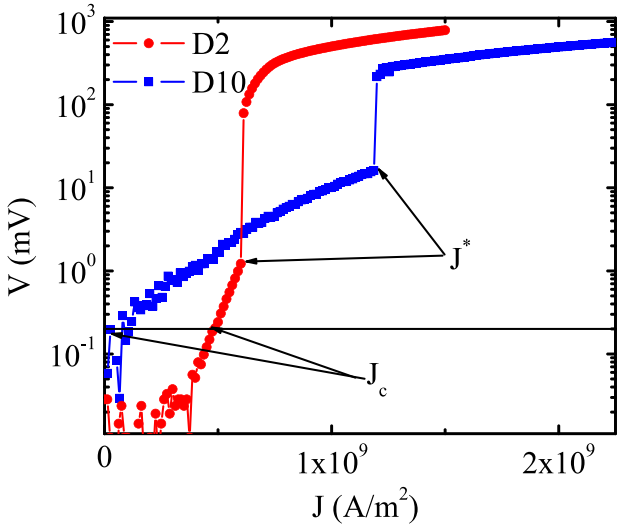

Fig. 7. J–V curves for microstrips D2 and D10 at $T = 2$ K and $\mu_0 H = 0.5$ T. The arrows indicate the values for J_c and J^* for both samples. The horizontal line indicates the adopted voltage criterion for the determination of J_c.

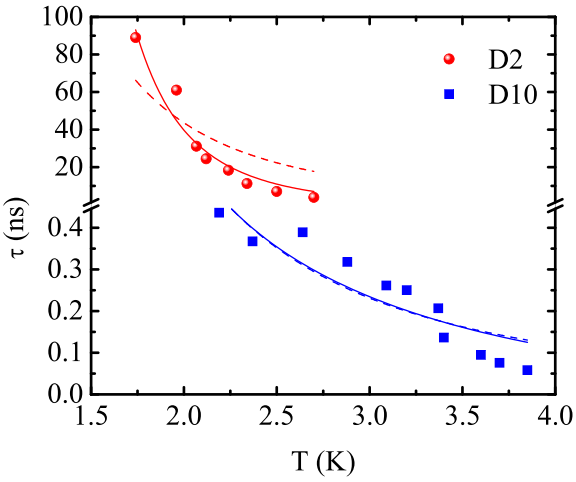

Fig. 8. Temperature dependence of the quasiparticle relaxation time for microstrips D2 (circles) and D10 (squares) at $\mu_0 H = 0.6$ T. The solid (dashed) lines represent the fitting curves to the data, employing the expressions for $\tau_E(T)$ valid in the case of the *ee* (*ep*) recombination mechanisms (see the text for further details).

have $\tau_E(T) \propto T^{-3}$ [64]. In Fig. 8, the temperature dependence of the quasiparticle relaxation time for microstrips D2 (circles) and D10 (squares) is shown for $\mu_0 H = 0.6$ T. The solid lines represent the curves $\tau_E(T) = \tau_0 \exp[m\Delta(T)/k_B T]$, where τ_0 and m have been determined as fitting parameters. The temperature dependence of the superconducting gap has been taken equal to $\Delta(T) = 1.76 k_B T_c \sqrt{\cos(\pi T^2/2T_c^2)}$, which is a good approximation of the Bardeen-Cooper-Schrieffer (BCS) type dependence over the entire temperature range from zero to T_c [65]. The dashed lines correspond to the best fit to the experimental data using the relation $\tau_E(T) = AT^{-n}$, with A and n as free parameters. For microstrip D2 the values of τ_E are two orders of magnitude larger and exhibit a more pronounced temperature dependence. In fact, they are well reproduced by the *ee* recombination mechanism with $\tau_0 = 3.64 \times 10^{-10}$ s and a smaller gap for the quasi particles, corresponding to $m = 1.35$, as shown by the solid red line in Fig. 8. A reduced value of the coefficient m in comparison to the BCS case (where $m = 2$) was previously observed in the context of the exponential temperature dependence of the relaxation time in a Nb/Py microstrip. However, this observation coincided with an increase in the critical velocity [54]. In our case the exponential behavior of $\tau_E(T)$ is found in correspondence of lower values of v^* which are likely due to the strong bulk pinning present in the microstrip [36,66]. The same data points can be equally well fitted with the *ep* expression for $\tau_E(T)$, but with the unphysical value $n = 6$ for the exponent. For comparison, we plot the dashed red line in Fig. 8 which represents the curve $\tau_E(T) = AT^{-n}$ with $n = 3$ and $A = 3.4 \times 10^{-7}$ s K^3. In this case, a more significant discrepancy with the experimental data is observed. In contrast, the data for sample D10 show a weak temperature dependence, in agreement with previous results [33]. In this case, the expressions for $\tau_E(T)$ reproduce two best-fit curves that are almost indistinguishable. However, in the case of *ee* relaxation (solid blue line in Fig. 8), the fit to the data does not yield reasonable numbers. We obtain $\tau_0 = 8.54 \times 10^{-11}$ s and $m = 0.52$, indicating a strongly reduced value of the BCS gap. In contrast, the fit to the data using $\tau_E(T) = AT^{-n}$ (dashed blue line in Fig. 8) gives $A = 8.54 \times 10^{-9}$ s K$^{2.3}$ and $n = 2.3$, close to the value $n = 3$, indicating reasonable agreement with the *ep* relaxation mechanism. Similar behavior with relaxation times of the same order of magnitude and nearly constant with temperature has been observed in NbRe. This result was attributed to the disordered nature of the material [32]. Likewise, low values for m and $n \sim 2$ were found in superconducting microstrips in contact with a ferromagnetic layer, coinciding with an increase in the critical velocity compared to the bare superconducting sample [38,67]. However, in the case of NbN/CuNi bilayer a reduction in J_c compared to pure NbN was also observed [38].

5. Conclusions

In conclusion, we have investigated the electric transport properties of NbReN microstrips of different quality by measuring I–V characteristics under an external magnetic field. Our primary goal was to estimate the quasiparticle relaxation time, aiming to understand the suitability of this material for use in SMSPDs. We observed that the values of τ_E strongly depend on the pinning properties of the samples, which have been carefully analyzed. Additionally, we found that the thickness and width of the strips also play a role, as evidenced by a larger value of J_c measured in the thick and narrow strip. This result is in agreement with previous observations in Nb bridges [45]. For the best strip, we estimated a value for τ_E as low as 12 ps at low fields and temperature. This value is similar to what was obtained at higher temperature with disordered NbN [68] but one order of magnitude lower than that obtained with disordered WSi,[69] NbGe,[70] and, recently, with γ-Mo_2N [71]. Furthermore, τ_E weakly depends on the temperature, indicating, as expected for highly-disordered superconducting systems, the predominant role of electron–phonon scattering compared to the electron–electron scattering. Our results altogether suggest that the right choice of parameters for the device geometry (with effects on J_c) combined with a tuning in the fabrication process and material growth (with effects on τ_E) should lead to NbReN SMSPDs with performance which could be even better than those of other SMSPDs reported to date.

CRediT authorship contribution statement

Z. Makhdoumi Kakhaki: Writing – review & editing, Investigation, Data curation. **A. Leo:** Investigation, Data curation. **A. Spuri:** Investigation, Data curation. **M. Ejrnaes:** Investigation. **L. Parlato:** Investigation. **G.P. Pepe:** Investigation, Funding acquisition. **F. Avitabile:** Data curation. **A. Di Bernardo:** Writing – review & editing, Methodology. **A. Nigro:** Writing – review & editing. **C. Attanasio:** Writing – review & editing, Writing – original draft, Supervision, Conceptualization. **C. Cirillo:** Writing – review & editing, Supervision, Resources, Conceptualization.

Declaration of competing interest

The authors declare that they have no known competing financial interests or personal relationships that could have appeared to influence the work reported in this paper.

Data availability

Data will be made available on request.

Acknowledgments

This research was supported by the QUANCOM Project (MUR PON Ricerca e Innovazione No. 2014–2020 ARS01_00734). This work is part of the project IR0000003 - IRIS supported by the NextGeneration EU-funded Italian National Recovery and Resilience Plan with the Decree of the Ministry of University and Research number 124 (21/06/2022) for the Mission 4 - Component 2 - Investment 3.1.

References

[1] G.N. Gol'tsman, O. Okunev, G. Chulkova, A. Lipatov, A. Semenov, K. Smirnov, B. Voronov, A. Dzardanov, C. Williams, R. Sobolewski, Picosecond superconducting single-photon optical detector, Appl. Phys. Lett. 79 (2001) 705.

[2] C.M. Natarajan, M.G. Tanner, R.H. Hadfield, Superconducting nanowire single-photon detectors: Physics and applications, Supercond. Sci. Technol. 25 (2012) 063001.

[3] I. Holzman, Y. Ivry, Superconducting nanowires for single-photon detection: Progress, challenges, and opportunities, Adv. Quantum Technol. 2 (2019) 1800058.

[4] H. Zhang, L. Xiao, B. Luo, J. Guo, L. Zhang, J. Xie, The potential and challenges of time-resolved single-photon detection based on current-carrying superconducting nanowires, J. Phys. D: Appl. Phys. 53 (2020) 013001.

[5] I.E. Zadeh, J. Chang, J.W.N. Los, S. Gyger, A.W. Elshaari, S. Steinhauer, S.N. Dorenbos, V. Zwiller, Superconducting nanowire single-photon detectors: A perspective on evolution, state-of-the-art, future developments, and applications, Appl. Phys. Lett. 118 (2021) 190502.

[6] L. You, Superconducting nanowire single-photon detectors for quantum information, Nanophotonics 9 (2020) 2673.

[7] A. Engel, J.J. Renema, K. Il'in, A. Semenov, Detection mechanism of superconducting nanowire single-photon detectors, Supercond. Sci. Technol. 28 (2015) 114003.

[8] N. Zen, A. Casaburi, S. Shiki, K. Suzuki, M. Ejrnaes, R. Cristiano, M. Ohkubo, 1 mm ultrafast superconducting stripline molecule detector, Appl. Phys. Lett. 95 (2009) 172508.

[9] A. McCarthy, N.J. Krichel, N.R. Gemmell, X. Ren, M.G. Tanner, S.N. Dorenbos, V. Zwiller, R.H. Hadfield, G.S. Buller, Kilometer-range, high resolution depth imaging via 1560 nm wavelength single-photon detection, Opt. Express 21 (2013) 8904.

[10] Y. Guan, H. Li, L. Xue, R. Yin, L. Zhang, H. Wang, G. Zhu, L. Kang, J. Chen, P. Wu, Lidar with superconducting nanowire single-photon detectors: Recent advances and developments, Opt. Lasers Eng. 156 (2022) 107102.

[11] Y. Hochberg, I. Charaev, S.-W. Nam, V. Verma, M. Colangelo, K.K. Berggren, Detecting sub-GeV dark matter with superconducting nanowires, Phys. Rev. Lett. 123 (2019) 151802.

[12] C. Zhang, W. Zhang, J. Huang, L. You, H. Li, C. Iv, T. Sugihara, M. Watanabe, H. Zhou, Z. Wang, X. Xie, NbN superconducting nanowire single-photon detector with an active area of 300μm-in-diameter, AIP Adv. 9 (2019) 075214.

[13] I.E. Zadeh, J.W.N. Los, R.B.M. Gourgues, V. Steinmetz, G. Bulgarini, S.M. Dobrovolskiy, V. Zwiller, S.N. Dorenbos, Single-photon detectors combining high efficiency, high detection rates, and ultra-high timing resolution, APL Photonics 2 (2017) 111301.

[14] F. Marsili, V.B. Verma, J.A. Stern, S. Harrington, A.E. Lita, T. Gerrits, I. Vayshenker, B. Baek, M.D. Shaw, R.P. Mirin, S.W. Nam, Detecting single infrared photons with 93% system efficiency, Nat. Photonics 7 (2013) 210.

[15] V.B. Verma, A.E. Lita, M.R. Vissers, F. Marsili, D.P. Pappas, R.P. Mirin, S.W. Nam, Superconducting nanowire single photon detectors fabricated from an amorphous $Mo_{0.75}Ge_{0.25}$ thin film, Appl. Phys. Lett. 105 (2014) 022602.

[16] M. Caloz, M. Perrenoud, C. Autebert, B. Korzh, M. Weiss, C. Schönenberger, R.J. Warburton, H. Zbinden, F. Bussiéres, High-detection efficiency and low-timing jitter with amorphous superconducting nanowire single-photon detectors, Appl. Phys. Lett. 112 (2018) 061103.

[17] C. Cirillo, J. Chang, M. Caputo, J.W.N. Los, S. Dorenbos, I.E. Zadeh, C. Attanasio, Superconducting nanowire single photon detectors based on disordered NbRe films, Appl. Phys. Lett. 117 (2020) 172602.

[18] A.N. Zotova, D.Y. Vodolazov, Photon detection by current-carrying superconducting film: A time-dependent Ginzburg–Landau approach, Phys. Rev. B 85 (2012) 024509.

[19] D. Yu Vodolazov, Single-photon detection by a dirty current-carrying superconducting strip based on the kinetic-equation approach, Phys. Rev. A 7 (2017) 034014.

[20] M. Ejrnaes, C. Cirillo, D. Salvoni, F. Chianese, C. Bruscino, P. Ercolano, A. Cassinese, C. Attanasio, G.P. Pepe, L. Parlato, Single photon detection in NbRe superconducting microstrips, Appl. Phys. Lett. 121 (2022) 262601.

[21] Y.P. Korneeva, D. Yu. Vodolazov, A.V. Semenov, I.N. Florya, N. Simonov, E. Baeva, A.A. Korneev, G.N. Goltsman, T.M. Klapwijk, Optical single-photon detection in micrometer-scale NbN bridges, Phys. Rev. A 9 (2018) 064037.

[22] J. Chiles, S.M. Buckley, A. Lita, V.B. Verma, J. Allmaras, B. Korzh, M.D. Shaw, J.M. Shainline, R.P. Mirin, S.W. Nam, Superconducting microwire detectors based on WSi with single-photon sensitivity in the near-infrared, Appl. Phys. Lett. 116 (2020) 242602.

[23] I. Charaev, Y. Morimoto, A. Dane, A. Agarwal, M. Colangelo, K.K. Berggren, Large-area microwire MoSi single-photon detectors at 1550 nm wavelength, Appl. Phys. Lett. 116 (2020) 242603.

[24] Y.P. Korneeva, N.N. Manova, I.N. Florya, M.Y. Mikhailov, O.V. Dobrovolskiy, A.A. Korneev, D. Yu. Vodolazov, Different single-photon response of wide and narrow superconducting Mo_xSi_{1-x} strips, Phys. Rev. A 13 (2020) 024011.

[25] G.Z. Xu, W.J. Zhang, L.X. You, J.M. Xiong, X.Q. Sun, H. Huang, X. Ou, Y.M. Pan, C.L. Lv, H. Li, Z. Wang, X.M. Xie, Superconducting microstrip single-photon detector with system detection efficiency over 90% at 1550 nm, Photonics Res. 9 (2021) 958.

[26] Y.P. Korneeva, N.N. Manova, M.A. Dryazgov, N.O. Simonov, P.I. Zolotov, A.A. Korneev, Influence of sheet resistance and strip width on the detection efficiency saturation in micron-wide superconducting strips and large-area meanders, Supercond. Sci. Technol. 34 (2021) 084001.

[27] M. Protte, V.B. Verma, J.P. Höpker, R.P. Mirin, S.W. Nam, T.J. Bartley, Laser-lithographically written micron-wide superconducting nanowire single-photon detectors, Supercond. Sci. Technol. 35 (2022) 055005.

[28] P. Ercolano, C. Cirillo, M. Ejrnaes, F. Chianese, D. Salvoni, C. Bruscino, R. Satariano, A. Cassinese, C. Attanasio, G.P. Pepe, L. Parlato, Investigation of dark count rate in NbRe microstrips for single photon detection, Supercond. Sci. Technol. 36 (2023) 105011.

[29] S.-Z. Lin, O. Ayala-Valenzuela, R.D. McDonald, L.N. Bulaevskii, T.G. Holesinger, F. Ronning, N.R. Weisse-Bernstein, T.L. Williamson, A.H. Mueller, M.A. Hoffbauer, M.W. Rabin, M.J. Graf, Characterization of the thin-film NbN superconductor for single-photon detection by transport measurements, Phys. Rev. B 87 (2013) 184507.

[30] A. Leo, P. Marra, G. Grimaldi, R. Citro, S. Kawale, E. Bellingeri, C. Ferdeghini, S. Pace, A. Nigro, Competition between intrinsic and extrinsic effects in the quenching of the superconducting state in Fe(Se, Te) thin films, Phys. Rev. B 93 (2016) 054503.

[31] M. Caputo, C. Cirillo, S. Voltan, A.M. Cucolo, J. Aarts, C. Attanasio, Influence of the magnetic configuration on the vortex-lattice instability in Nb/permalloy bilayers, Phys. Rev. B 96 (2017) 174519.

[32] M. Caputo, C. Cirillo, C. Attanasio, NbRe as candidate material for fast single photon detection, Appl. Phys. Lett. 111 (2017) 192601.

[33] C. Cirillo, V. Granata, A. Spuri, A. Di Bernardo, C. Attanasio, NbReN: A disordered superconductor in thin film form for potential application as superconducting nanowire single photon detector, Phys. Rev. Mater. 5 (2021) 085004.

[34] O.V. Dobrovolskiy, D. Yu Vodolazov, F. Porrati, R. Sachser, V.M. Bevz, M. Yu Mikhailov, A.V. Chumak, M. Huth, Ultra-fast vortex motion in a direct-write Nb-C superconductor, Nature Commun. 11 (2020) 3291.

[35] G. Blatter, M. Sirena, N. Haberkorn, Enhancement of the vortex critical velocity in superconducting/normal metal bilayers, Mater. Sci. Eng. B 299 (2024) 116943.

[36] B. Budinská, B. Aichner, D. Yu. Vodolazov, M. Yu. Mikhailov, F. Porrati, M. Huth, A.V. Chumak, W. Lang, O.V. Dobrovolskiy, Rising speed limits for fluxons via edge-quality improvement in wide MoSi thin films, Phys. Rev. A 17 (2022) 034072.

[37] A.I. Larkin, Yu N. Ovchinnikov, Nonlinear conductivity of superconductors in the mixed state, Sov. Phys.—JETP 41 (1976) 960.

[38] C. Cirillo, V. Pagliarulo, H. Myoren, C. Bonavolontà, L. Parlato, G.P. Pepe, C. Attanasio, Quasiparticle energy relaxation times in NbN/CuNi nanostripes from critical velocity measurements, Phys. Rev. B 84 (2011) 054536.

[39] C. Attanasio, C. Cirillo, Quasiparticle relaxation mechanisms in superconductor/ferromagnet bilayers, J. Phys.: Condens. Matter 24 (2012) 083201.

[40] L. Zhang, L. You, W. Penga, Z. Wang, Quasiparticle scattering time in NbN superconducting thin films, Physica C 579 (2020) 1353773.

[41] P.H. Kes, C.C. Tsuei, Two-dimensional collective flux pinning, defects, and structural relaxation in amorphous superconducting films, Phys. Rev. B 28 (1983) 5126.

[42] Z. Makhdoumi Kakhaki, A. Leo, F. Chianese, L. Parlato, G.P. Pepe, A. Nigro, C. Cirillo, C. Attanasio, Upper critical magnetic field in NbRe and NbReN micrometric strips, Beilstein J. Nanotechnol. 14 (2023) 45.

[43] N.R. Werthamer, E. Helfand, P.C. Hohenberg, Temperature and purity dependence of the superconducting critical field, H_{c2}. III. Electron spin and spin-orbit effects, Phys. Rev. 147 (1966) 295.
[44] B.L.T. Plourde, D.J. Van Harlingen, D. Yu. Vodolazov, R. Besseling, M.B.S. Hesselberth, P.H. Kes, Influence of edge barriers on vortex dynamics in thin weakpinning superconducting strips, Phys. Rev. B 64 (2001) 014503.
[45] K. Il'in, D. Rall, M. Siegel, A. Engel, A. Schilling, A. Semenov, H.-W. Huebers, Influence of thickness, width and temperature on critical current density of Nb thin film structures, Physica C 470 (2010) 953.
[46] K. Ilin, D. Henrich, Y. Luck, Y. Liang, M. Siegel, D. Yu Vodolazov, Critical current of Nb, NbN, and TaN thin-film bridges with and without geometrical nonuniformities in a magnetic field, Phys. Rev. B 89 (2014) 184511.
[47] G.M. Maksimova, Mixed state and critical current in narrow semiconducting films, Phys. Sol. Stat. 40 (1998) 1607.
[48] H. Yamasaki, K. Endo, S. Kosaka, M. Umeda, S. Yoshida, K. Kajimura, Scaling of the flux pinning force in epitaxial $Bi_2Sr_2Ca_2Cu_30_x$ thin films, Phys. Rev. Lett. 70 (1993) 3331.
[49] S.L. Prischepa, C. Attanasio, C. Coccorese, L. Maritato, F. Pourtier, M. Salvato, V.N. Kushnir, Temperature scaling of the flux pinning force in $Bi_2Sr_2Ca_1Cu_2O_{8+x}$ thin films, J. Appl. Phys. 79 (1996) 4228.
[50] E. Martínez, P. Mikheenko, M. Martínez-López, A. Millán, A. Bevan, J.S. Abell, Flux pinning force in bulk MgB2 with variable grain size, Phys. Rev. B 75 (2007) 134515.
[51] Md. Matin, L.S. Sharath Chandra, M.K. Chattopadhyay, R.K. Meena, Rakesh Kaul, M.N. Singh, A.K. Sinha, S.B. Roy, Magnetic irreversibility and pinning force density in the Ti-V alloys, J. Appl. Phys. 113 (2013) 163903.
[52] D. Dew-Hughes, Flux pinning mechanisms in type II superconductors, Phil. Mag. 30 (1974) 293.
[53] B.J. Ruck, H.J. Trodahl, J.C. Abele, M.J. Geselbracht, Dynamic vortex instabilities in Ta/Ge-based multilayers and thin films with various pinning strengths, Phys. Rev. B 62 (2000) 12468.
[54] A. Angrisani Armenio, C. Bell, J. Aarts, C. Attanasio, High-velocity instabilities in the vortex lattice of Nb/permalloy bilayers, Phys. Rev. B 76 (2007) 054502.
[55] A.V. Samoilov, M. Konczykowski, N.-C. Yeh, S. Berry, C.C. Tsuei, Electric-field-induced electronic instability in amorphous Mo_3Si superconducting films, Phys. Rev. Lett. 75 (1995) 4118.
[56] J. Romijn, T.M. Klapwijk, M.J. Renne, J.E. Mooij, Critical pair-breaking current in superconducting aluminum strips far below T_c, Phys. Rev. B 26 (1982) 3648.
[57] M.Y. Kupriyanov, V.F. Lukichev, Temperature dependence of pair-breaking current in superconductors, Sov. J. Low Temp. Phys. 6 (1980) 210.
[58] S. Doettinger, R. Huebener, A. Kühle, Electronic instability during vortex motion in cuprate superconductors regime of low and high magnetic fields, Physica C 251 (1995) 285.
[59] S.G. Doettinger, S. Kittelberger, R.P. Huebener, C.C. Tsuei, Quasiparticle energy relaxation in the cuprate superconductors, Phys. Rev. B 56 (1997) 14157.
[60] G. Grimaldi, A. Leo, D. Zola, A. Nigro, S. Pace, F. Laviano, E. Mezzetti, Evidence for low-field crossover in the vortex critical velocity of type-II superconducting thin films, Phys. Rev. B 82 (2010) 024512.
[61] X. Chen, C. Cirillo, M. Ejrnaes, L. Parlato, G.P. Pepe, C. Attanasio, S.J. van der Molen, M.J.A. de Dood, Vortex motion study of oxidised superconducting NbRe microstrips, IEEE Trans. Appl. Supercond. (2023) http://dx.doi.org/10.1109/TASC.2023.3340641.
[62] A.V. Silhanek, A. Leo, G. Grimaldi, G.R. Berdiyorov, M.V. Milošević, A. Nigro, S. Pace, N. Verellen, W. Gillijns, V. Metlushko, B. Ilić, Xiaobin Zhu, V.V. Moshchalkov, Influence of artificial pinning on vortex lattice instability in superconducting films, New J. Phys. 14 (2012) 053006.
[63] S.B. Kaplan, C.C. Chi, D.N. Langenberg, J.J. Chang, S. Jafarey, D.J. Scalapino, Quasiparticle and phonon lifetimes in superconductors, Phys. Rev. B 14 (1976) 4854.
[64] A.I. Larkin, Yu N. Ovchinnikov, Nonlinear effects during the motion of vortices in superconductors, Sov. Phys.—JETP 46 (1977) 155.
[65] T.P. Sheahen, Rules for the energy gap and critical field of superconductors, Phys. Rev. 149 (1966) 368.
[66] S.S. Ustavschikov, M. Yu. Levichev, I. Yu. Pashenkin, A.M. Klushin, D. Yu. Vodolazov, Approaching depairing current in dirty thin superconducting strip covered by low resistive normal metal, Supercond. Sci. Technol. 34 (2021) 015004.
[67] C. Cirillo, E.A. Ilyina, C. Attanasio, Static and dynamic properties of the vortex lattice in superconductor/weak ferromagnet bilayers, Supercond. Sci. Technol. 24 (2011) 024017.
[68] M. Sidorova, A. Semenov, H.-W. Hübers, K. Ilin, M. Siegel, I. Charaev, M. Moshkova, N. Kaurova, G.N. Goltsman, X. Zhang, A. Schilling, Electron energy relaxation in disordered superconducting NbN films, Phys. Rev. B 102 (2020) 054501.
[69] M.V. Sidorova, A.G. Kozorezov, A.V. Semenov, Yu. P. Korneeva, M. Yu. Mikhailov, A. Yu. Devizenko, A.A. Korneev, G.M. Chulkova, G.N. Goltsman, Nonbolometric bottleneck in electron–phonon relaxation in ultrathin WSi films, Phys. Rev. B 97 (2018) 184512.
[70] D. Babić, J. Bentner, C. Sürgers, C. Strunk, Flux-flow instabilities in amorphous $Nb_{0.7}Ge_{0.3}$ microbridges, Phys. Rev. B 69 (2004) 092510.
[71] J.A. Hofer, M. Ginzburg, S. Bengio, N. Haberkorn, Nanocrystalline superconducting γ-Mo_2n ultra-thin films for single photon detectors, Mater. Sci. Eng. B 275 (2022) 115499.